

Electronically Passivated Hole-Blocking Titanium Dioxide/Silicon Heterojunction for Hybrid Silicon Photovoltaics

Gabriel Man,* Jeffrey Schwartz, James C. Sturm, and Antoine Kahn*

Carrier-selective heterojunctions are important for low-cost silicon-based photovoltaic applications. A low temperature (<100 °C) chemical vapor deposition technique is used here to deposit ultrathin (n-type) titanium dioxide (TiO₂) layers onto hydrogen-passivated surfaces of crystalline-silicon (c-Si). Energy level alignment and chemical composition at these abrupt, interfacial layer-free TiO₂/Si heterojunctions are investigated via ultraviolet, X-ray, and inverse photoemission spectroscopy, for c-Si doping ranging from p⁺⁺(10¹⁹) to n⁺⁺(10¹⁹). The interface Fermi level position and device-relevant TiO₂/Si band offsets are found to shift monotonically as a function of the Si doping, revealing the absence of Fermi level pinning at the c-Si interface and pointing to simple Fermi level equilibration as the driving mechanism behind the interface energy level alignment. Electrical transport measurements performed on TiO₂/Si-based diodes confirm the energy level alignment yielded by spectroscopic measurements and the hole-blocking properties of the TiO₂/Si heterojunction, exclude hole conduction in the TiO₂ as a transport mechanism, and show carrier recombination at the TiO₂/p-Si heterojunction.

1. Introduction

Silicon-based heterojunctions are of great importance for photovoltaic applications. From a technological standpoint, carrier-selective contacts to silicon are appealing since they offer a potentially lower-cost alternative to p–n homojunctions. Crystalline-silicon (c-Si) solar cells have reached high power conversion efficiencies, but the required p–n junctions are expensive to fabricate since high-purity furnaces operating at over 800 °C are required. One solution is the amorphous-silicon/crystalline-silicon (a-Si/c-Si) heterojunction concept, which is employed in silicon heterojunction-with-intrinsic-thin-layer (HIT) cells.^[1] The downside of HIT cells is the reduction of the short-circuit current due to parasitic absorption in the a-Si carrier-selective and passivation layers,^[2] and requirement of plasma-enhanced deposition methods (for the amorphous silicon). Alternative interlayers involving wider band gap materials have therefore

been investigated. Because of its nontoxicity, corrosion resistance, optical transparency to the visible spectrum, and favorable positions of its energy levels of relevance to electronic devices, titanium dioxide (TiO₂) has been heavily utilized in all-inorganic and hybrid inorganic/organic optoelectronic devices as a carrier-selective interlayer.^[3–6] With an expected band gap of ≈3.2 eV for TiO₂ versus ≈1.7 eV for a-Si, the TiO₂/silicon (TiO₂/Si) heterojunction is expected to offer all of the advantages of the HIT, with less parasitic absorption and possibly simpler deposition methods.

The formation of electronic-grade heterojunctions on crystalline inorganic semiconductors like silicon is always a challenge due to electronically active defects resulting from interfacial chemical interactions and unsaturated dangling bonds.^[7] Defects lead to interface gap states and Fermi level pinning, which affect band

offsets across heterojunctions, and act as carrier recombination centers. Simple Fermi level equilibration as the energy level alignment mechanism is rarely observed in all-inorganic heterojunctions, while it is more commonly observed in chemically inert and electronically weak interacting classes of interfaces such as organic/organic and organic/metal-oxide heterojunctions.^[8] The highly successful SiO₂/c-Si and a-Si/c-Si heterojunctions remain today among the few examples of nearly defect-free interfaces on Si.

TiO₂ layers as carrier-selective interlayers in inorganic, organic, or hybrid semiconductor solar cells are generally grown via atomic layer deposition (ALD),^[5,9,10] chemical vapor deposition (CVD),^[11,12] or solution-based processes.^[13,14] These and other growth techniques have been used to deposit both crystalline and amorphous TiO₂ layers on Si. Mixed results are typically observed in terms of interface electronic structures, which are strongly affected by defects and sensitively dependent on the initial silicon surface preparation and the processing conditions.^[15]

We have recently demonstrated the formation of an electronic-grade TiO₂/c-Si heterojunction by deposition of a thin, smooth, and pin-hole free layer (few nm) of amorphous TiO₂ via condensation of titanium tetra(*tert*-butoxide) precursor molecules on hydrogen-passivated Si (H-Si) cooled below room temperature, followed by a mild annealing at 100 °C to thermolyze the *tert*-butoxide ligands and cross-link the resulting Ti–OH species.^[3,4] These “as-deposited” TiO₂ layers, grown on the electron-collection side of a crystalline n-Si solar cell, were

G. Man, Prof. J. C. Sturm, Prof. A. Kahn
Department of Electrical Engineering
Princeton University
Princeton, NJ 08544, USA
E-mail: gman@princeton.edu; kahn@princeton.edu
Prof. J. Schwartz
Department of Chemistry
Princeton University
Princeton, NJ 08544, USA



DOI: 10.1002/admi.201600026

shown to serve as an effective electron collection pathway and hole blocker that essentially maintained the electronic integrity of the passivated Si interface, with low interface defect density and carrier recombination velocity.^[16]

With the present study, our aim is to provide an in-depth investigation of the electronic band alignment and electrical transport properties of the aforementioned TiO₂/c-Si heterojunction with as-deposited TiO₂ layers. The combined interface and device study of the abrupt, interfacial layer-free TiO₂/c-Si heterojunction demonstrates the absence of interface Fermi level pinning, a characteristic of an electronically passivated interface. Simple Fermi level equilibration is revealed to be the driving mechanism behind the energy level alignment. The hole-blocking property of the TiO₂/Si heterojunction is confirmed via electrical transport measurements, which is consistent with other reports.^[3,5,17] No evidence for hole conduction through the n-type TiO₂ is found. Carrier recombination is revealed as an important transport mechanism at TiO₂/p-Si heterojunctions.

2. Results and Discussion

2.1. Electronic and Optical Characterization of the Titanium Dioxide

The electronic structure of as-deposited TiO₂ films is investigated using a combination of ultraviolet photoemission spectroscopy (UPS) and inverse photoemission spectroscopy (IPES) (Figure 1). Our previously published work showed UPS Helium I and IPES spectra measured on 1–4 nm thick TiO₂ on Si.^[18,19] Both spectra included some contributions from the underlying silicon, which complicated the determination of the valence and conduction band edges of TiO₂. The development of a process for depositing thicker (10–15 nm) TiO₂ films, coupled with the use of more surface-sensitive UPS Helium II (as compared to Helium I), enables a more accurate determination of

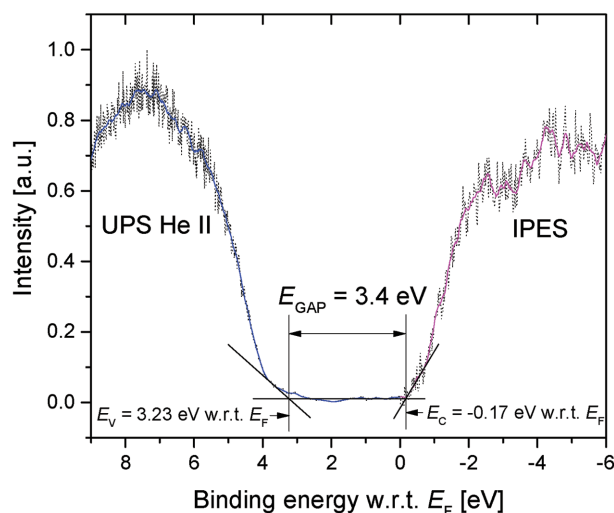


Figure 1. Combined UPS Helium II and IPES spectra of as-deposited TiO₂, showing the transport gap E_{GAP} . The energy reference (0 eV) corresponds to the position of the Fermi level E_{F} .

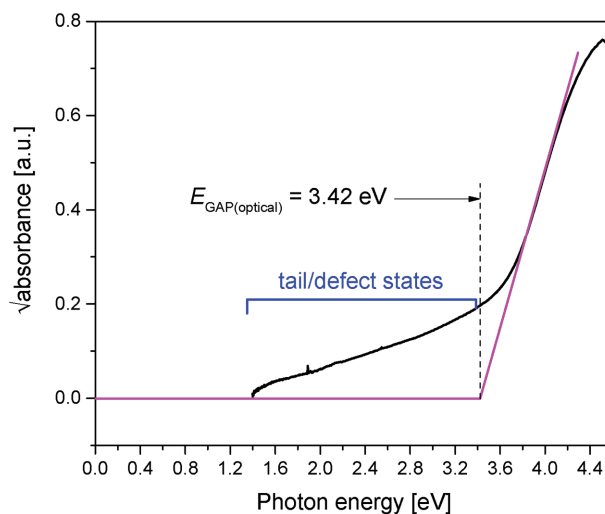


Figure 2. UV-vis absorption spectra of ≈ 5 nm of as-deposited TiO₂ on glass, showing the optical gap $E_{\text{GAP(optical)}}$.

the electronic structure of TiO₂. Under typical deposition conditions, TiO₂ is an n-type material doped by oxygen vacancies (deep donors) and/or titanium interstitials (shallow donors).^[20] This is confirmed here by the position of the Fermi level (E_{F}) close to the conduction band minimum $E_{\text{C}}(\text{TiO}_2)$. The work function of as-deposited TiO₂, $\phi(\text{TiO}_2)$, measured from the photoemission cut-off (not shown here), is 4.0 ± 0.1 eV. The valence band maximum $E_{\text{V}}(\text{TiO}_2)$ is at 3.2 eV below E_{F} , giving an ionization energy of 7.2 ± 0.2 eV. Conversely, $E_{\text{C}}(\text{TiO}_2)$ is at 0.2 ± 0.2 eV above E_{F} , giving an electron affinity (EA) of 3.8 ± 0.3 eV and a band gap of 3.4 ± 0.3 eV. Tezuka et al. previously used a combination of X-ray photoemission spectroscopy (XPS) and IPES to establish a band gap of 3.3 ± 0.5 eV for rutile TiO₂.^[21] Although there is a spread of values in the literature, the general consensus is that the band gaps of crystalline rutile and anatase TiO₂ are 3.03 and 3.20 eV, respectively.^[22] The slightly larger band gap reported in this work could be due to the noncrystalline phase of the as-deposited TiO₂, which is grown at a maximum temperature of 100 °C. Typical amorphous-to-crystalline-anatase transitions occur at ≈ 300 °C. A small density of states extending above $E_{\text{V}}(\text{TiO}_2)$ into the gap corresponds to tail states, which can also be seen in the optical absorption spectra of TiO₂ on glass (Figure 2).

A 3.42 eV optical gap is extracted from the absorption spectrum of TiO₂. This value compares well to the above transport gap (3.4 ± 0.3 eV), since the exciton binding energy in (rutile) TiO₂ is on the order of 5 meV.^[23] The magenta fit in Figure 2 corresponds to the expected spectrum if the optical absorption originated solely from an interband transition.^[24] However, as the actual spectrum shows, there is substantial subgap absorption due to a distribution of tail/defect states.

2.2. Spectroscopic Measurements of the Titanium Dioxide/Silicon Heterojunction Band Offsets

XPS was used to probe the chemical composition of the TiO₂/Si interface. The silicon 2p (Si2p) core level spectra for various

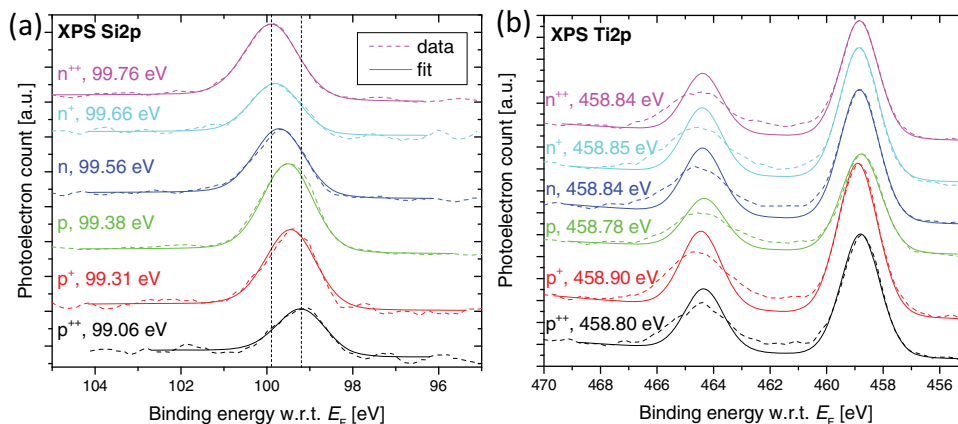


Figure 3. XPS spectra of the a) silicon 2p and b) titanium 2p core levels, for as-deposited TiO₂ on a variety of n-Si and p-Si substrates. The peak positions are given for the Si and Ti 2p_{3/2} peaks. The data are plotted in dashed lines, and the peak fits are represented by solid lines.

TiO₂/Si heterojunctions, featuring n-Si and p-Si ranging in doping concentration from 10¹⁶ to 10¹⁹ cm⁻³, are shown in Figure 3a. The Si2p peaks were fitted with 20% Lorentzian, 80% Gaussian peaks with a spin-orbit splitting of 0.4 eV between the Si2p_{1/2} and Si2p_{3/2} peaks. The Ti2p_{1/2} and Ti2p_{3/2} components were fitted with the same Lorentzian:Gaussian ratio as the Si2p peaks, and a spin-orbit splitting of 5.54 eV.^[25] The Ti2p core level spectra (Figure 3b) indicates that titanium is in its +4 oxidation state, as shown previously.^[3] In all cases, the Si2p peak corresponding to bulk silicon dominates the spectra, indicating that the interface has not undergone a chemical reaction and is spatially abrupt. This is in contrast with TiO₂/Si interfaces formed via less gentle and higher temperature processes, which have shown the presence of combinations of titanium silicides, titanium oxides, and silicon oxides of various stoichiometries.^[26–28]

Schlom et al. state that a chemical reaction between Si and TiO₂ is energetically favorable since the volume free energy change ΔG is negative.^[29] This suggests that irrespective of how the interface is formed, a chemical reaction will occur at higher temperature. Indeed, our own experiments on the TiO₂/Si heterojunction show evidence for Si–O–Ti bonding at the interface (not shown here), after the heterojunction is annealed at 250 °C for 3 min in an inert atmosphere.^[17] The formation of a mixed silicon/titanium oxide interfacial layer appears to be kinetically limited.

XPS was also used to elucidate the electronic band alignment at each TiO₂/Si heterojunction using the Kraut method.^[30] Indeed, the short mean free path of XPS photoelectrons precludes the direct measurement of the Si valence band edge through the TiO₂ layer, and use is made of the larger probing depth of XPS for the Si 2s and 2p core levels. First, the spatial region probed by the XPS measurements must be clarified. At the soft X-ray photon energy used (1486.7 eV), photoelectrons originating from the Ti2p and Si2p

core levels have kinetic energies of ≈ 1000 and ≈ 1400 eV, respectively. From the standard universal curve of inelastic mean free path (IMFP) versus electron kinetic energy, the IMFPs of Ti2p and Si2p photoelectrons are ≈ 2 and ≈ 2.5 nm, respectively.^[31] Attenuation of the photoelectron signal follows an exponential distribution into the solid, starting at the free surface of the solid. In essence, XPS Ti2p measurements probe the topmost ≈ 4 nm of the TiO₂ (at 4 nm, $e^{-2} \approx 0.1$), and XPS Si2p measurements probe the Si energy levels in the top ≈ 4 nm of the Si. These points are summarized in Figure 4 by the measurement windows in red.

To utilize the Kraut method, the energy offset between a Si or Ti core level and E_V of separate Si or TiO₂ layers was established. Following interface formation, measured energy differences between the chosen Si and Ti core levels were used to yield the heterojunction ΔE_V (and ΔE_C since the band gaps are known) band offsets. As shown in Figure 4, the measured band offsets are determined by the difference between the TiO₂ energy

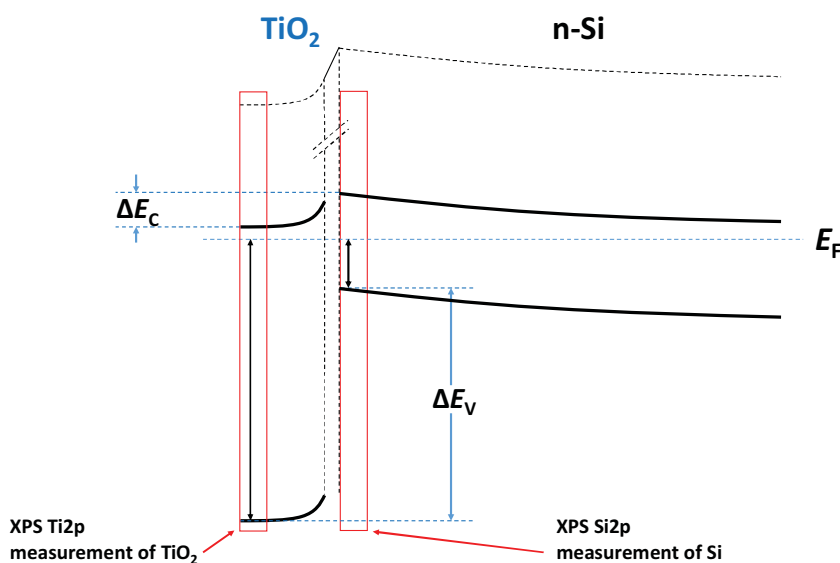


Figure 4. Band diagram showing the regions probed by XPS measurements in red, and the measured valence and conduction band offsets.

levels in the vicinity of the free TiO₂ surface, and the Si energy levels near the interface. Consequently, the measured band offsets are the sum of the abrupt band offsets right at the TiO₂/Si interface and band bending in the TiO₂ from the near surface to the interface. However, as we will show, they are still very much relevant for carrier injection/extraction in TiO₂/Si-based devices. Henceforth, the band offsets will be referred to explicitly and implicitly as device-relevant band offsets. The Ti2p core level was chosen for its larger photoionization cross-section (at the soft X-ray photon energy used, 1486.7 eV) as compared to the other Ti core levels.^[32] The Si 2p and 2s core levels have the largest photoionization cross-sections, which are comparable in magnitude. In order to determine $E_{\text{Si}2\text{p}_{3/2}}(\text{Si}) - E_{\text{V}}(\text{Si})$, and given the unknown density of states at the valence band top of the H-passivated Si surface, initially H-passivated n⁺Si(10¹⁸) and p⁺Si(10¹⁸) samples were argon-ion sputtered in high vacuum to induce a large density of surface states, which are known to pin the Fermi level at ≈0.4 eV above $E_{\text{V}}(\text{Si})$ regardless of the doping type.^[33] Confirming this point, the same energy position of 99.38 eV below E_{F} was found for the Si2p_{3/2} peak in both cases (n⁺ and p⁺), yielding a value for $E_{\text{Si}2\text{p}_{3/2}}(\text{Si}) - E_{\text{V}}(\text{Si})$ of 98.95 eV, comparable to values reported by others.^[34] For the $E_{\text{Ti}2\text{p}_{3/2}}(\text{TiO}_2) - E_{\text{V}}(\text{TiO}_2)$ offset, the energy position of $E_{\text{V}}(\text{TiO}_2)$ with respect to E_{F} , obtained from UPS Helium II measurements, was subtracted from $E_{\text{Ti}2\text{p}_{3/2}}(\text{TiO}_2)$ with respect to E_{F} , obtained from XPS measurements. The resulting $E_{\text{Ti}2\text{p}_{3/2}}(\text{TiO}_2) - E_{\text{V}}(\text{TiO}_2)$ offset ranged from 455.38 to 455.77 eV. The average of the offset values —455.58 eV—was used.

The density of charged surface states on the H-Si surface only, prior to TiO₂ deposition, is estimated from the Si band bending. Measurements of $E_{\text{Si}2\text{p}_{3/2}}(\text{Si})$ for H-n⁺Si(10¹⁸) and H-p⁺Si(10¹⁸) yield values of 99.73 and 99.15 eV, respectively. Band bending in Si is obtained from the energy difference between $E_{\text{V}}(\text{Si})$ at the interface and in the bulk. The interface position with respect to E_{F} is deduced from the Si2p core level energy. The bulk position is calculated by taking the lower bound of the resistivity range, obtaining the equivalent doping concentration, and calculating the energy position of E_{F} using

the Maxwell–Boltzmann approximation.^[35] The bands bend ≈0.2 eV down for H-p⁺Si, and ≈0.3 eV up for H-n⁺Si. To estimate the surface state/defect density, we calculate the total charge contained in the Si depletion region using the standard width W of the depletion region

$$W = \sqrt{\frac{2\varepsilon V_0}{qN_d}} \quad (1)$$

Taking H-n⁺Si as an example, and using values of $\varepsilon = 11.8 \times 8.854 \times 10^{-14}$ F cm⁻¹, $V_0 = 0.3$ V, $q = 1.602 \times 10^{-19}$ C, $N_d = 1 \times 10^{18}$ cm⁻³, the depletion region is estimated to be 1.98×10^{-6} cm or ≈20 nm wide. The silicon surface state density, obtained by multiplying the bulk doping concentration by the depletion region width, is estimated to be ≈ 2×10^{12} states cm⁻². H-Si prepared with simple wet chemical processing in ambient conditions yields therefore reasonably low surface state densities, with ≈1 defect per 350 atoms at the surface.

XPS measurements (Figure 3) were performed on a series of TiO₂/Si heterojunctions, for Si n- and p-doping ranging in concentration from 10¹⁶ to 10¹⁹ cm⁻³. Using the Kraut method described above, these measurements yield the complete energy diagrams of these heterojunctions as shown in Figure 5. Measured and derived values are summarized in Table 1. The key result is the shift of the Fermi level at the Si surface, showing the absence of Fermi level pinning, as the silicon doping evolves progressively from p⁺⁺ to n⁺⁺. The TiO₂ energy levels shift monotonically with respect to those of Si, as exemplified by the heterojunction valence band offset, which changes from 3.11 eV for TiO₂/p⁺⁺Si to 2.45 eV for TiO₂/n⁺⁺Si. Recall that the measured ΔE_{V} is the energy difference between $E_{\text{V}}(\text{TiO}_2)$ at the free surface of the TiO₂ and $E_{\text{V}}(\text{Si})$ at the interface. Irrespective of the bulk Si doping type and concentration, the Fermi level in the band gap of TiO₂ is always positioned at ≈0.1–0.2 eV below $E_{\text{C}}(\text{TiO}_2)$, confirming the n-type character of as-deposited TiO₂. There is no observable asymmetry in any of the Ti2p peaks (comparing the Ti2p_{3/2} peak spectra and curve fit; Figure 3b), which indicates that the energy levels are flat in the ≈4 nm of

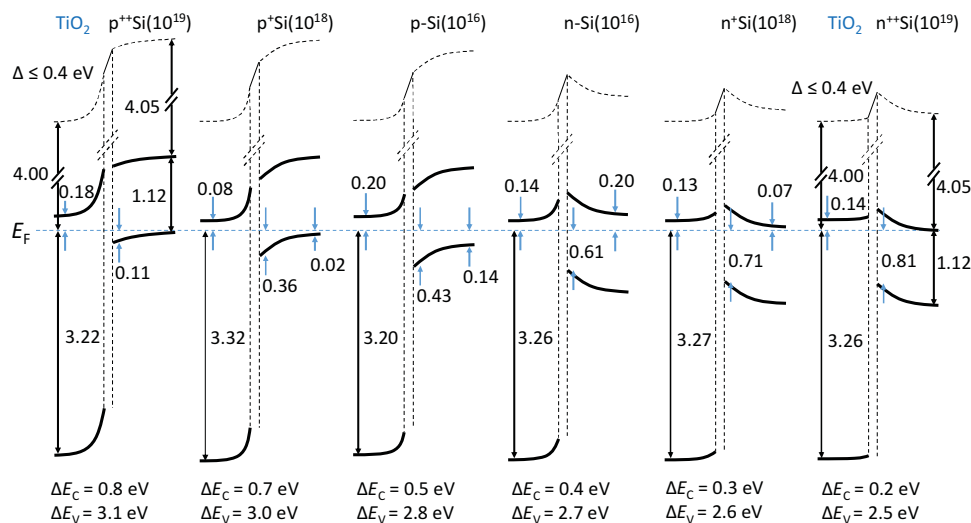


Figure 5. Heterojunction interface dipole and device-relevant band offsets of as-deposited TiO₂ on a variety of n-Si and p-Si. The vacuum level is shown as a dashed line to visually aid the reader, as it does not actually exist in the bulk of a solid.

Table 1. Summary of TiO₂/Si interface dipole Δ and device-relevant band offsets (all values in eV).

	TiO ₂ /p ⁺ Si(10 ¹⁹)	TiO ₂ /p ⁺ Si(10 ¹⁸)	TiO ₂ /p-Si(10 ¹⁶)	TiO ₂ /n-Si(10 ¹⁶)	TiO ₂ /n ⁺ Si(10 ¹⁸)	TiO ₂ /n ⁺ Si(10 ¹⁹)
$\phi(\text{TiO}_2)$				4.00		
$E_{\text{GAP}}(\text{TiO}_2)$				3.40		
$E_{\text{F}} - E_{\text{Si}2\text{p}3/2}$	99.06	99.31	99.38	99.56	99.66	99.76
$E_{\text{F}} - E_{\text{V}}(\text{Si})$	0.11	0.36	0.43	0.61	0.71	0.81
$E_{\text{C}}(\text{Si}) - E_{\text{F}}$	-1.01	-0.76	-0.69	-0.51	-0.41	-0.31
$V_{\text{BB}}(\text{Si})$	0.11	0.34	0.29	0.31	0.34	0.31
$E_{\text{F}} - E_{\text{Ti}2\text{p}3/2}$	458.80	458.90	458.78	458.84	458.85	458.84
$E_{\text{F}} - E_{\text{V}}(\text{TiO}_2)$	3.22	3.32	3.20	3.26	3.27	3.26
$E_{\text{C}}(\text{TiO}_2) - E_{\text{F}}$	-0.18	-0.08	-0.20	-0.14	-0.13	-0.14
ΔE_{V}	3.11	2.96	2.77	2.65	2.56	2.45
ΔE_{C}	0.83	0.68	0.49	0.37	0.28	0.17
Δ				≤ 0.4		

TiO₂ near the free surface. There are two implications associated with this finding. First, there is a negligible surface state density at the free surface of the TiO₂, otherwise band bending would be present. Second, if a depletion region originating from charge transfer to/from the Si or interface states is present in the 10–15 nm thick TiO₂ films, its width is <10 nm. The absence of Fermi level pinning at the c-Si interface results from the chemical/hydrogen passivation of silicon, which remains largely intact throughout the TiO₂ deposition process,^[17] and the absence of intrinsic interface-induced gap states.^[36] These measurements show that Fermi level equilibration is the primary mechanism behind the TiO₂/Si band alignment.

A contact potential difference (CPD) between TiO₂ and doped H-Si is expected. Regardless of whether the underlying H-Si is doped p- or n-type, the work function of the TiO₂ overlayer ranges from 3.9 to 4.1 eV, according to UPS measurements. The electron affinity of H-Si is derived from UPS measurements of $\phi(\text{H-Si})$, XPS measurements of $E_{\text{V}}(\text{Si})$ with respect to E_{F} , and the known band gap of Si. EA(H-Si) values are found to range from 3.9 to 4.2 eV. Average values of 4.0 and 4.05 eV for $\phi(\text{TiO}_2)$ and EA(H-Si), respectively, will be used in the subsequent analysis. The presence of an intrinsic interface dipole is expected since Si and TiO₂ possess different electronegativity values. The magnitude of the intrinsic interface dipole, Δ , is proportional to the difference in electronegativities.^[36] The TiO₂/n⁺Si(10¹⁹) heterojunction, with the smallest expected CPD, is used to estimate an upper bound to the magnitude of the interfacial dipole. Assuming minimal band bending in the TiO₂ at the TiO₂/n⁺Si interface, the Δ is ≤ 0.4 eV, as shown in Figure 5. The series of heterojunctions feature the same abrupt, interfacial layer-free TiO₂/Si interface; hence, Δ will be the same for the entire series. For both n-Si and p-Si, the direction of Δ points toward the Si, which is different from the findings of Hu et al.^[28]

The heterojunctions investigated here which are most relevant to silicon-based photovoltaics are TiO₂/p-Si(10¹⁶) and TiO₂/n-Si(10¹⁶). As can be seen in Figure 5, the TiO₂/p-Si(10¹⁶) heterojunction features a depletion region, which can separate photogenerated carriers in silicon and is consistent with the photovoltaic effect observed previously.^[3,19] Electronically

passivated TiO₂/n-Si heterojunctions have been reported by us and others.^[16,37]

2.3. Current–Voltage Measurements on TiO₂/Si-Based Diodes

The TiO₂/Si band alignments shown in Figure 5 were tested against electrical transport measurements (J – V) carried out on Al/TiO₂/Si/Ag diode structures for all corresponding doping types and concentrations. Al/n-Si and Al/p-Si Schottky diodes were used as control devices. The latter comprise a metal/semiconductor interface typically dominated by Fermi level pinning caused by metal-induced-gap states and defects. The absence of Fermi level pinning at the TiO₂/Si interface can be readily observed from the Al/TiO₂/n-Si-based diodes, while the hole-blocking properties of the heterojunction can be observed from the Al/TiO₂/p-Si-based diodes. The absence of hole conduction through the n-type TiO₂, and the presence of carrier recombination at the TiO₂/p-Si heterojunction, is also observed from the Al/TiO₂/p-Si-based diodes.

The J – V characteristics of Al/n-Si(10¹⁶), Al/TiO₂/n-Si(10¹⁶), and Al/TiO₂/n⁺Si(10¹⁸) diodes are shown in Figure 6a,b. Fifteen devices of each type were tested and the figure reflects characteristic representatives of these data. The electron barrier height of an Al/n-Si Schottky junction is known to be ≈ 0.7 eV.^[38] As expected, the corresponding J – V characteristics (Figure 6b) are strongly rectifying. In n-Si(10¹⁶), the bulk $E_{\text{C}}(\text{Si}) - E_{\text{F}}$ is ≈ 0.2 eV, giving a band bending of ≈ 0.5 V for the Schottky junction. The band bending for the unpinned TiO₂/n-Si(10¹⁶) and TiO₂/n⁺Si(10¹⁸) interfaces was measured to be ≈ 0.3 V (Figure 5). This difference is clearly reflected in the forward biased J – V characteristics, with a faster rise in current for the Al/TiO₂/n-Si and Al/TiO₂/n⁺Si diodes compared to the Al/n-Si(10¹⁶) Schottky diode (Figure 6a). At forward bias voltages of +0.8 V and above, where the Al/TiO₂/n-Si(10¹⁶) and Al/n-Si(10¹⁶) diodes are series resistance limited, the current in the Al/n-Si diode exceeds that in the Al/TiO₂/n-Si diode, likely due to the increased series resistance introduced by the TiO₂ layer. In reverse bias, the electron injection barrier at the Al/TiO₂/n-Si and Al/TiO₂/n⁺Si heterojunctions is significantly smaller than that at the Al/n-Si

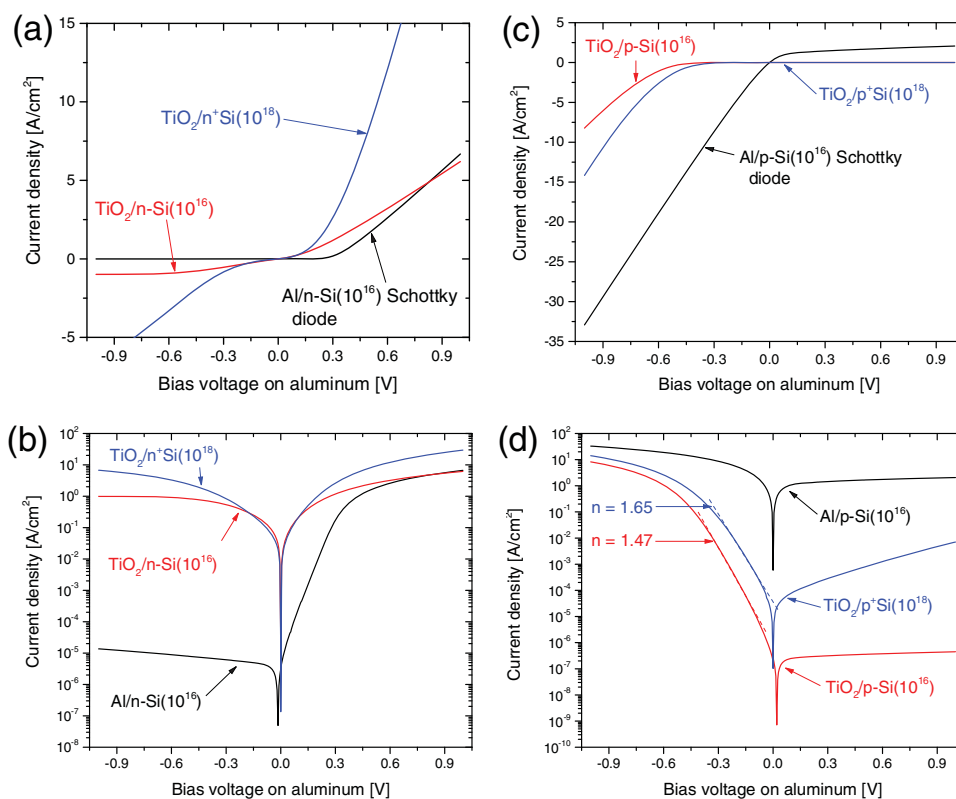


Figure 6. Linear-scale and semi-log J - V characteristics of representative Al/n-Si(10^{16}) Schottky, Al/TiO₂/n-Si(10^{16}), Al/TiO₂/p⁺Si(10^{18}), Al/p-Si(10^{16}) Schottky, Al/TiO₂/p-Si(10^{16}), and Al/TiO₂/p⁺Si(10^{18}) diodes.

Schottky junction, resulting in orders of magnitude larger reverse saturation current density. Our findings are qualitatively consistent with both those of Avasthi et al. and Agrawal et al., who also demonstrated the absence of Fermi level pinning at the TiO₂/Si interface via electrical transport measurements on TiO₂/n-Si-based diodes, demonstrating either ohmic or reduced barrier behavior.^[3,39] Schematic band diagrams summarizing current mechanisms for the Al/TiO₂/n-Si(10^{16}) diode in forward and reverse bias are shown at the top of Figure 7.

The J - V characteristics of Al/p-Si(10^{16}), Al/TiO₂/p-Si(10^{16}), and Al/TiO₂/p⁺Si(10^{18}) diodes are shown in Figure 6c,d. As mentioned previously, the electron barrier height for the Al/Si Schottky junction is typically ≈ 0.7 eV. With a room temperature silicon band gap of 1.12 eV, the hole injection barrier height is relatively small, ≈ 0.4 eV. Indeed, the J - V curve of the Al/p-Si diode reflects nearly ohmic behavior in forward bias, indicative of a very small Schottky barrier. In contrast, we observe the Al/TiO₂/p-Si diode to be highly rectifying, with a very low reverse current, similar to ref. [3]. In reverse bias, the deep valence band of TiO₂ precludes any hole injection from the aluminum electrode into the p-Si, and the reverse saturation current is six orders of magnitude lower than in the Al/p-Si diode. Hu et al. have reported on the existence of a

defect band centered at ≈ 1.3 eV below $E_C(\text{TiO}_2)$, which consequently could make the ALD-deposited TiO₂ “leaky” and facilitates hole conduction through the barrier.^[28] If present in our results, we should observe some bias-dependent hole current for the reverse-biased Al/TiO₂/p-Si diode. The reverse current density for the diode is essentially bias independent; hence, hole conduction through the TiO₂ is excluded as a transport mechanism. Differences in the TiO₂ growth and processing (i.e., 150 °C ALD vs 100 °C CVD) may lead to the differing characteristics.

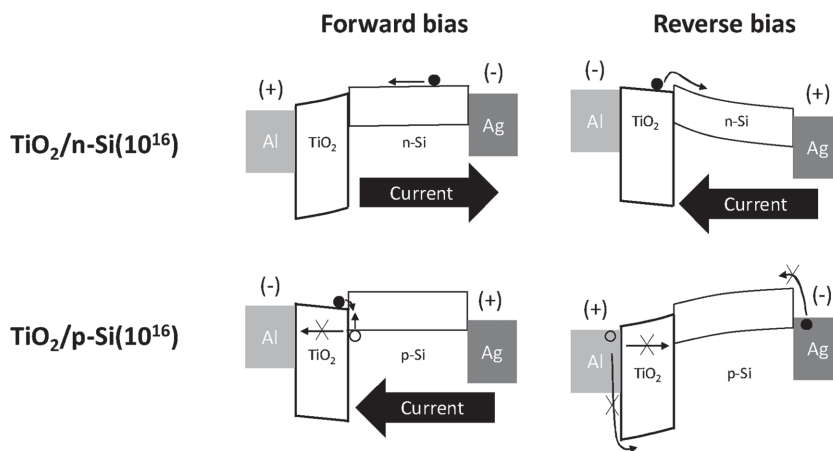


Figure 7. Expected electrical transport mechanisms for Al/TiO₂/n-Si(10^{16}) and Al/TiO₂/p-Si(10^{16}) heterojunction diodes.

In forward bias, the large ΔE_V at the TiO₂/p-Si heterojunction (Figure 5) is expected to block hole extraction at the aluminum contact. However, the Al/TiO₂/p-Si diode does conduct in forward bias, and hole conduction through the TiO₂ has been excluded by the reverse bias case. Thus electron injection from the metal through the TiO₂ conduction band into the p-Si is present. The ideality factor n of the J - V is ≈ 1.5 , signifying that the main current mechanism is not electron injection into the bulk silicon (which would exhibit $n = 1$), but rather carrier recombination in the silicon depletion region, or more likely, at the TiO₂/p-Si interface. Current mechanisms for the Al/TiO₂/p-Si(10^{16}) diode in forward and reverse bias are shown in Figure 7.

3. Conclusion

We presented a greatly expanded investigation of the electronic structure of a TiO₂/crystalline-Si system previously used as a hole blocker in efficient Si solar cells. The thin (10–15 nm) oxide layer is deposited using a low temperature (<100 °C) CVD method that largely preserves the chemical/hydrogen passivation of the Si(100) surface. As the Si doping concentration and type are progressively changed from p⁺⁺(10^{19}) to n⁺⁺(10^{19}), the silicon energy band position at the TiO₂/Si interface changes by ≈ 0.7 eV according to photoemission spectroscopy measurements, unequivocally demonstrating that the Fermi level at the interface is not pinned. Consequently, Fermi level equilibration between the naturally n-doped oxide and Si is found to be the driving mechanism behind the heterojunction energy level alignment. As the substrate doping changes progressively as above, we demonstrate a monotonic and controllable shift of the TiO₂ energy levels ≈ 10 nm away from the interface of up to ≈ 0.7 eV with respect to those of Si. Electrical transport measurements show that the large band gap and deep valence band edge of TiO₂ insures the formation of an efficient hole-blocking carrier-selective interlayer at the electron-collection contact of the Si solar cell, and that gap states at the interface may play a role in the remaining current mechanisms.

4. Experimental Section

Sample Preparation: Single-side polished, 300 or 500 μm thick, native-oxide covered silicon(100) wafers were used as starting substrates. Six different types of doping were used: n⁺⁺Si (0.001–0.003 $\Omega\text{ cm}$, $\approx 2 \times 10^{19}\text{ cm}^{-3}$), n⁺Si (0.01–0.02 $\Omega\text{ cm}$, $2 \times 10^{18}\text{ cm}^{-3}$), n-Si (0.3–0.5 $\Omega\text{ cm}$, $1 \times 10^{16}\text{ cm}^{-3}$), p-Si (0.1–0.5 $\Omega\text{ cm}$, $4 \times 10^{16}\text{ cm}^{-3}$), p⁺Si (0.01–0.02 $\Omega\text{ cm}$, $4 \times 10^{18}\text{ cm}^{-3}$), and p⁺⁺Si (0.001–0.005 $\Omega\text{ cm}$, $2 \times 10^{19}\text{ cm}^{-3}$). Silicon wafer cleaning was performed with the standard two-step Radio Corporation of America (RCA) wafer clean.^[40] After the second and final HF etch (30 s in 20:1 H₂O:HF), the hydrogen-passivated silicon samples were inserted into the TiO₂ deposition chamber with <1 min of air exposure during transport. TiO₂ deposition was carried out with a home-built CVD system; the organometallic precursor was titanium(IV) *tert*-butoxide, purchased from STREM Chemicals (Newburyport, MA). The deposition process was derived from a method used to deposit TiO₂ onto polymer substrates.^[41] The CVD system used in this work was functionally similar to the system used in the previous work,^[3,4,16,19]

except now a precursor bulb with a larger diameter is used, which increases the rate of injection of precursor into the deposition chamber, leading to thicker TiO₂ films. Adsorption of the precursor vapor occurred at a base temperature and a pressure of -10 °C and 15 mTorr, respectively. After adsorption, the substrate was heated up to 100 °C to decompose the precursor (thermolysis) and form the TiO₂ film. Typical TiO₂ film thicknesses prepared using this technique ranged between 10 and 15 nm, according to spectroscopic ellipsometry measurements. The TiO₂/Si samples were typically exposed to air for <5 min, while being transported to the vacuum system for spectroscopy measurements, or to the thermal evaporator for diode fabrication.

Spectroscopy Measurements: UPS, XPS, and IPES measurements were carried out in a dedicated ultra-high vacuum (UHV) chamber with a base pressure of $<2 \times 10^{-10}$ Torr. UPS was performed with both the Helium I (21.22 eV) and Helium II (40.81 eV) photon lines, generated by a Specs gas discharge lamp. Satellite lines in the UPS spectra were carefully removed. The work function was extracted from the onset of photoemission (high binding energy cut-off) in UPS Helium I spectra, following a well-established procedure. XPS was performed with non-monochromatized aluminum-K α X-rays at 1486.7 eV, and the XPSPeak software was used for peak fitting the spectra. A double-pass cylindrical mirror analyzer was used in UPS and XPS. IPES was performed in the isochromat mode with a home-built setup.^[42] The energy resolution of UPS, XPS, and IPES were 0.15, 0.80, and 0.45 eV, respectively. Alignment of the energy scales for the three techniques was accomplished by using the energy position of the Fermi edge measured on a sputter-cleaned gold film in UHV.

Electrical Transport Measurements: Silver/aluminum/TiO₂/silicon/silver diode structures were fabricated for perpendicular transport measurements. Arrays of circular metallic pads, consisting of 20 nm of aluminum and 200 nm of silver, were thermally evaporated onto the TiO₂ through shadow masks, using an Edwards 306 evaporator. The diameter of the pads was 0.5 mm, which yielded a top contact area of $\approx 2 \times 10^{-3}\text{ cm}^2$. Current spreading was not expected to be an issue, and the device area was effectively the same as the top contact area.^[3] The back-side contact was a 200 nm thick blanket layer of silver evaporated onto scribed silicon. A typical sample contained up to 90 diodes, and the representative J - V was taken from the middle of the J - V distribution. Electrical measurements were performed inside a nitrogen-filled glovebox, and a thin and flexible gold wire, mounted on a micromanipulator, was used to make electrical contact to the top pad. An Agilent 4155B semiconductor parameter analyzer, connected via General Purpose Interface Bus (GPIB) to a PC running LabVIEW, was used to execute the voltage sweeps and acquire the I - V data.

Other Characterization: UV-vis absorption spectroscopy was performed on an Agilent 8453 UV-vis-NIR spectrometer. A clean glass slide was used for the background measurement. A J. A. Woollam M-2000 spectroscopic ellipsometer was used to acquire ellipsometry data on minimally air-exposed TiO₂/Si samples, and the thicknesses of the TiO₂ films were obtained by fitting the spectroscopic data to a vendor-supplied Tauc-Lorentz oscillator model for TiO₂.

Acknowledgements

This work was supported by the DOE Sunshot Grant No. DE-EE0005315. G.M. acknowledges partial financial support from the Natural Sciences and Engineering Research Council of Canada (NSERC). G.M. thanks the Central New Jersey branch of the IEEE for partial financial support of the construction of the TiO₂ deposition chamber. The authors thank Melda Sezen for assistance with UV-vis measurements, Ken Nagamatsu for preparing the TiO₂ film on glass, and Samuel French from SRI for providing crystalline-TiO₂ samples for reference PES measurements.

Received: January 11, 2016

Revised: March 24, 2016

Published online: May 4, 2016

- [1] M. Taguchi, A. Yano, S. Tohoda, K. Matsuyama, Y. Nakamura, T. Nishiwaki, K. Fujita, E. Maruyama, *IEEE J. Photovolt.* **2014**, *4*, 96.
- [2] Z. C. Holman, M. Filipič, A. Descoedres, S. De Wolf, F. Smole, M. Topi, C. Ballif, *J. Appl. Phys.* **2013**, *113*, 013107.
- [3] S. Avasthi, W. E. McClain, G. Man, A. Kahn, J. Schwartz, J. C. Sturm, *Appl. Phys. Lett.* **2013**, *102*, 203901.
- [4] K. A. Nagamatsu, S. Avasthi, G. Sahasrabudhe, G. Man, J. Jhaveri, A. H. Berg, J. Schwartz, A. Kahn, S. Wagner, J. C. Sturm, *Appl. Phys. Lett.* **2015**, *106*, 123906.
- [5] H. Kim, K.-L. Ou, X. Wu, P. F. Ndione, J. Berry, Y. Lambert, T. Mélin, N. R. Armstrong, S. Graham, *J. Mater. Chem. A* **2015**, *3*, 17332.
- [6] K. Morii, M. Ishida, T. Takashima, T. Shimoda, Q. Wang, M. K. Nazeeruddin, M. Grätzel, *Appl. Phys. Lett.* **2006**, *89*, 183510.
- [7] W. G. Oldham, A. G. Milnes, *Solid-State Electron.* **1964**, *7*, 153.
- [8] M. T. Greiner, M. G. Helander, W.-M. Tang, Z.-B. Wang, J. Qiu, Z.-H. Lu, *Nat. Mater.* **2012**, *11*, 76.
- [9] X. Yin, C. Battaglia, Y. Lin, K. Chen, M. Hettick, M. Zheng, C.-Y. Chen, D. Kiriya, A. Javey, *ACS Photonics* **2014**, *1*, 1245.
- [10] L. Kavan, N. Tétreault, T. Moehl, M. Grätzel, *J. Phys. Chem. C* **2014**, *118*, 16408.
- [11] K.-L. Ou, D. Tadytin, K. X. Steirer, D. Placencia, M. Nguyen, P. Lee, N. R. Armstrong, *J. Mater. Chem. A* **2013**, *1*, 6794.
- [12] M. Thelakkat, C. Schmitz, H. W. Schmidt, *Adv. Mater.* **2002**, *14*, 577.
- [13] C. Waldauf, M. Morana, P. Denk, P. Schilinsky, K. Coakley, S. A. Choulis, C. J. Brabec, *Appl. Phys. Lett.* **2006**, *89*, 233517.
- [14] A. Yella, L.-P. Heiniger, P. Gao, M. K. Nazeeruddin, M. Grätzel, *Nano Lett.* **2014**, *14*, 2591.
- [15] C. C. Fulton, G. Lucovsky, R. J. Nemanich, *Appl. Phys. Lett.* **2004**, *84*, 580.
- [16] J. Jhaveri, S. Avasthi, K. Nagamatsu, J. C. Sturm, in *Proc. 40th IEEE Photovoltaic Specialists Conf.* **2014**, p. 1525, IEEE, Denver, CO.
- [17] G. Sahasrabudhe, S. M. Rupich, J. Jhaveri, A. H. Berg, K. A. Nagamatsu, G. Man, Y. J. Chabal, A. Kahn, S. Wagner, J. C. Sturm, J. Schwartz, *J. Am. Chem. Soc.* **2015**, *137*, gg14842.
- [18] J. Sturm, S. Avasthi, K. Nagamatsu, J. Jhaveri, W. E. McClain, G. Man, A. Kahn, J. Schwartz, S. Wagner, *ECS Trans.* **2013**, *58*, 97.
- [19] J. Jhaveri, S. Avasthi, G. Man, W. E. McClain, K. Nagamatsu, A. Kahn, J. Schwartz, J. C. Sturm, in *2013 IEEE 39th Photovoltaic Specialists Conf. (PVSC)*, **2013**, pp. 3292–3296, IEEE, Tampa, FL.
- [20] M. K. Nowotny, P. Bogdanoff, T. Dittrich, S. Fiechter, A. Fujishima, H. Tributsch, *Mater. Lett.* **2010**, *64*, 928.
- [21] Y. Tezuka, S. Shin, T. Ishii, T. Ejima, S. Suzuki, S. Sato, *J. Phys. Soc. Jpn.* **1994**, *63*, 347.
- [22] D. O. Scanlon, C. W. Dunnill, J. Buckeridge, S. A. Shevlin, A. J. Logsdail, S. M. Woodley, C. R. A. Catlow, M. J. Powell, R. G. Palgrave, I. P. Parkin, G. W. Watson, T. W. Keal, P. Sherwood, A. Walsh, A. A. Sokol, *Nat. Mater.* **2013**, *12*, 798.
- [23] *Landolt-Börnstein—Group III Condensed Matter 41D (Non-Tetrahedrally Bonded Binary Compounds II)*, No. 41D (Eds: O. Madelung, U. Rössler, M. Schulz), Springer-Verlag, Berlin, **2000**.
- [24] J. Pankove, *Optical Processes in Semiconductors*, Dover Publications Inc., New York, NY, **1975**.
- [25] J. Moulder, W. Stickle, P. Sobol, K. Bomben, *Handbook of X-Ray Photoelectron Spectroscopy*, Physical Electronics, Inc., Eden Prairie, MN, **1995**.
- [26] L. J. Brillson, M. L. Slade, H. W. Richter, H. VanderPlas, R. T. Fulks, *J. Vac. Sci. Technol. A* **1986**, *4*, 993.
- [27] J. Abad, C. Rogero, J. Méndez, M. F. López, J. A. Martín-Gago, E. Román, *Surf. Sci.* **2006**, *600*, 2696.
- [28] S. Hu, M. Richter, M. F. Lichtenman, J. A. Beardslee, T. Mayer, B. S. Brunschwig, N. S. Lewis, *J. Phys. Chem. C* **2015**, *120*, 3117.
- [29] D. G. Schlom, C. A. Billman, J. H. Haeni, J. Lettieri, P. H. Tan, R. R. M. Held, S. Volk, K. J. Hubbard, in *Thin Films and Heterostructures for Oxide Electronics* (Ed: S. B. Ogale), Springer, **2005**, pp. 31–78, New York, NY.
- [30] E. Kraut, R. Grant, J. Waldrop, S. Kowalczyk, *Phys. Rev. Lett.* **1980**, *44*, 1620.
- [31] M. P. Seah, W. A. Dench, *Surf. Interface Anal.* **1979**, *1*, 2.
- [32] J. J. Yeh, I. Lindau, *At. Data Nucl. Data Tables* **1985**, *32*, 1.
- [33] F. J. Himpsel, G. Hollinger, R. A. Pollak, *Phys. Rev. B* **1983**, *28*, 7014.
- [34] S. Hu, M. R. Shaner, J. A. Beardslee, M. Lichtenman, B. S. Brunschwig, N. S. Lewis, *Science* **2014**, *344*, 1005.
- [35] R. S. Muller, T. I. Kamins, *Device Electronics for Integrated Circuits*, John Wiley & Sons, Hoboken, NJ, **2003**.
- [36] W. Monch, *Electronic Properties of Semiconductor Interfaces*, Springer-Verlag, Berlin **2004**.
- [37] B. Liao, B. Hoex, A. G. Aberle, D. Chi, C. S. Bhatia, *Appl. Phys. Lett.* **2014**, *104*, 253903.
- [38] H. C. Card, *IEEE Trans. Electron Devices* **1976**, *23*, 538.
- [39] A. Agrawal, J. Lin, M. Barth, R. White, B. Zheng, S. Chopra, S. Gupta, K. Wang, J. Gelatos, S. E. Mohny, S. Datta, *Appl. Phys. Lett.* **2014**, *104*, 8.
- [40] W. Kern, *J. Electrochem. Soc.* **1990**, *137*, 1887.
- [41] T. J. Dennes, J. Schwartz, *ACS Appl. Mater. Interfaces* **2009**, *1*, 2119.
- [42] C. I. Wu, Y. Hirose, H. Sirringhaus, A. Kahn, *Chem. Phys. Lett.* **1997**, *272*, 43.